Hindawi
Mathematical Problems in Engineering
Volume 2019, Article ID 2614327, 8 pages
https://doi.org/10.1155/2019/2614327

Research Article

Application Research of Chaotic Carrier Frequency Modulation Technology in Two-Stage Matrix Converter

Kai Wang, Liwei Li, Yong Lan, Peng Dong, and Guoting Xia

School of Electrical Engineering, Qingdao University, Qingdao 266071, China

Correspondence should be addressed to Kai Wang; wkwj888@163.com

Received 2 August 2018; Revised 8 January 2019; Accepted 7 February 2019; Published 6 March 2019

Academic Editor: Ruben Specogna

The harmonics of line to line voltage in two-stage matrix converter (TSMC) with fixed carrier frequency had discrete and high values and produced powerful electromagnetic interference (EMI). In this paper, chaotic carrier frequency modulation technique (CCFMT) was applied in TSMC for the first time to spread sideband range and suppress harmonic peak value. Although this technique could suppress EMI, it would increase the probability of narrow pulses. In order to improve reliability, the rectifier in the two-stage matrix converter uses PWM modulation with zero vector to extend the zero current commutation time, solves the narrow pulse problem, and simplifies the commutation process. At last, an experiment platform was designed and experimental results showed that harmonics of line to line voltage was efficiently suppressed.

1. Introduction

TSMC is a kind of direct AC/AC converters, which consists of rectifier and inverter with no filter capacitors. Apart from the advantages of matrix converter, TSMC also possesses some outstanding features, for instance, zero current commutation of rectifier, simple clamping circuit, and less switches at particular condition. Therefore, TSMC has become one of the most promising areas in many fields [1–6].

However, due to the fixed carrier frequency, the harmonics which appear at integer multiples of the carrier frequency of TSMC line to line voltage possess discrete and high values and produce powerful EMI. In order to meet the demands of electromagnetic compatibility (EMC), output filter should be adopted, which not only increases the volume and weight but also produces additional harmonics [7–11]. CCMFT is one of the most effective solutions of Carrier Frequency Modulation Technique (CFMT). It can make the carrier frequency change according to chaotic principle and spread the sideband to the whole frequency range; thus the harmonic peak value is effectively suppressed [12–19]. However, because there is no DC energy storage element, the rectifier and inverter should adopt collaborative commutation to modulate the fundamental component of the input current and output voltage

at the same carrier frequency. In a practical application, TSMC can generate narrow pulses inevitably and CCFMT also increases the possibility of producing them, which can lead to commutation failure and device damage [20–29].

In response to these shortcomings, we propose a new CCFMT which can improve commutation reliability. It can solve the narrow pulse problem and simplify the commutation process. In addition, we demonstrate the effectiveness and superiority of the proposed CCFMT to suppress EMI of TSMC on TSMC experiment platform [30–35].

Figure 1 shows the topology of TSMC with 18 switches. Because the input side of rectifier and output side of inverter have the properties of voltage source and current source, respectively, to ensure safe operation three principles should be as follows: prevent short circuit of three rectifier bridges, avoid direct connection between rectifier bridges, and prevent open circuit of inverter output side during rectifier commutation.

In this paper, we adopt chaotic carrier frequency. The carrier frequency f_s is as follows:

$$f_s = f_c + \Delta f_s x_k \quad (1)$$

In the equation, f_c is the constant carrier frequency; $\triangle f_s$ is the maximum offset; x_k is the chaotic iterative sequence. We

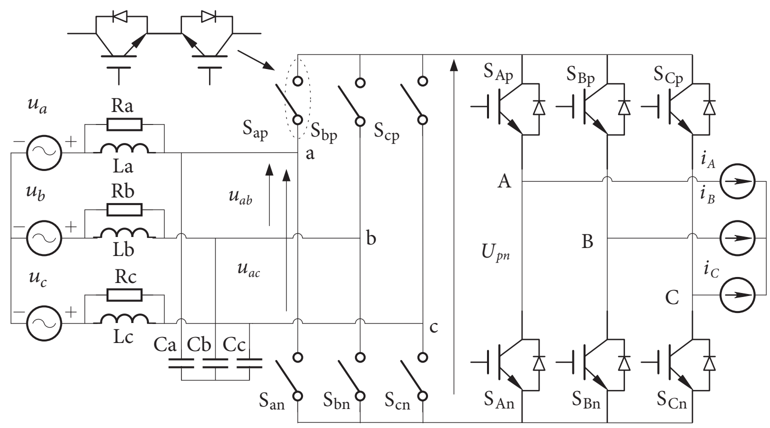

Figure 1: Topology of TSMC.

utilize Logistic sequence is a widely used chaotic mathematical model. This paper uses it to generate chaotic signals, and the recursive expression is as follows:

$$x_{k+1} = 1 - 2{x_k}^2, \quad x_k \in (-1, 1) \tag{2}$$

In working process, if same carrier frequency, appropriate rectifier carrier, and both modulation function and carrier wave of inverter are adopted, unnecessary commutation and switching operation can be avoided.

When the carrier frequency changes according to chaotic principle, the switching moment will be uncertain. It brings about irregularly distributed narrow pulses due to decreasing commutation time as the carrier period shortens. Although some enlarged carrier periods can remove the corresponding narrow pulses, CCFMT will increase the narrow pulses generally. The rectifier zero vector action time (ZVAT) is large at the transition of sectors. Thus if rectifier zero vector is employed, we can extend the commutation time, remove the influence of narrow pulses, and improve commutation reliability. Based on that, we propose a new CCFMT to improve the commutation reliability of TSMC [36–41].

2. The CCFMT Principle of TSMC

Suppose the normalized form of expected three-phase input current is as follows:

$$\begin{aligned} i_a &= \cos(\theta_i) \\ i_b &= \cos\left(\theta_i - \frac{2\pi}{3}\right) \\ i_c &= \cos\left(\theta_i + \frac{2\pi}{3}\right) \end{aligned} \tag{3}$$

In the equation, $\theta_i = \omega_i t$, ω_i is the angular frequency of input current. We divide the input current into 6 sectors, and the principle is that in each sector the direction of one certain current is opposite to the other two. Figure 2 shows the space vectors of input current. In Figure 2, $\mathbf{i}_\alpha$ and $\mathbf{i}_\beta$ are the working vectors of reference vector $\mathbf{i}$ in each sector. It can be obtained that if the input vector of the input current is different, the corresponding switching states of the rectifier are also different [20, 21]. To obtain the modulation function containing rectifier zero vector, the expression of $\mathbf{i}_\alpha$, $\mathbf{i}_\beta$ and duty ratio of ZVAT are as follows:

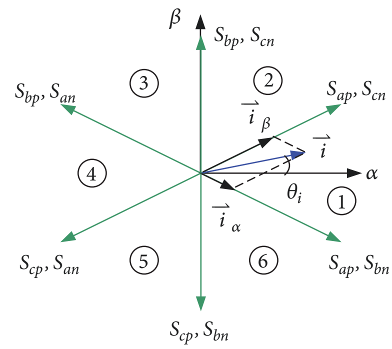

Figure 2: Space vectors of input current.

$$\begin{aligned} d_\alpha &= m_i \cos\left(\theta_i - \frac{k_i \pi}{3}\right) \\ d_\beta &= m_i \sin\left(\frac{k_i \pi}{3} - \theta_i - \frac{\pi}{6}\right) \\ d_0 &= 1 - d_\alpha - d_\beta \end{aligned} \tag{4}$$

In the equation, d_α, d_β, and d_0 are action time duty radios of $\mathbf{i}_\alpha$, $\mathbf{i}_\beta$, and zero vector, respectively; $m_i \in (0, 1.1547)$ is the modulation coefficient of rectifier, and $m_i = 1$ in this paper; $k_i = 1, 2, \ldots, 6$ is the number of input current sector.

The definitions of i_1 and i_2 are as follows:

$$\begin{aligned} i_1 &= d_\alpha \\ i_2 &= d_\alpha + d_0 \end{aligned} \tag{5}$$

In Figures 3(a) and 3(b), the longitudinal area between two modulation functions is ZVAT. In working process, rectifier will not output the switching states of zero vectors, which means that the DC-side voltage is still composed of two input

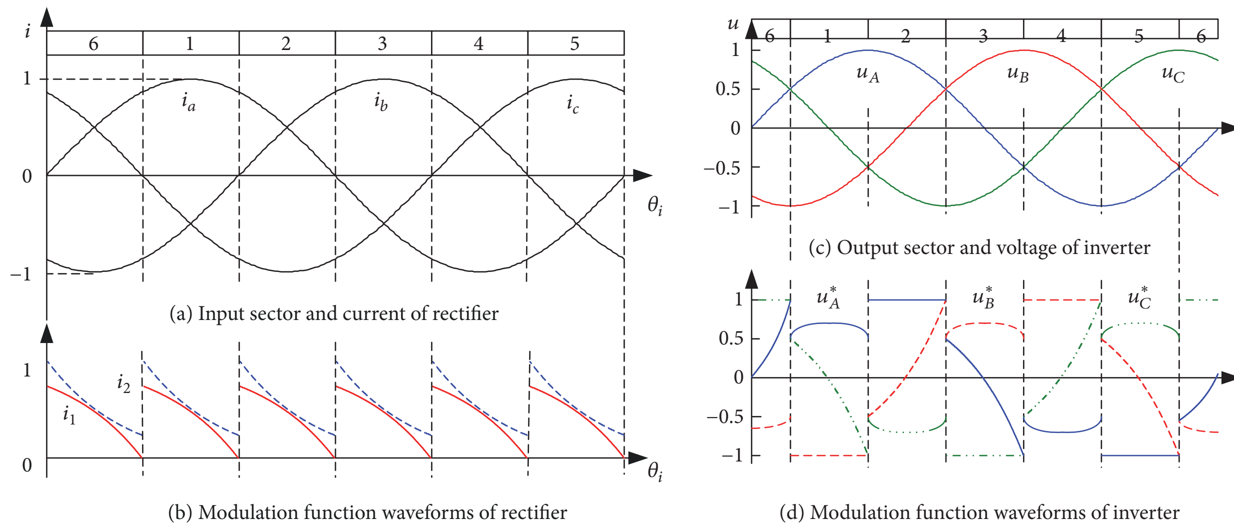

FIGURE 3: Waveforms of rectifier and inverter.

line voltages. The duty radio of the action time of each line voltage can be obtained from

$$\begin{aligned} d_1 &= d_\alpha + h_i d_0 \\ d_2 &= d_\beta + (1 - \mathrm{h}_i)\,\mathrm{d}_0 \end{aligned} \tag{6}$$

In the equation, $h_{\mathrm{i}} \in (0,1)$ is the distribution coefficient of ZVAT between two line voltages. We take $h_{\mathrm{i}} = 0.5$, and then the zero vector is distributed evenly. Suppose the normalized form of expected three-phase output current of inverter is as follows:

$$\begin{aligned} u_A &= \cos(\theta_o) \\ u_B &= \cos\left(\theta_o - \frac{2\pi}{3}\right) \\ u_C &= \cos\left(\theta_o + \frac{2\pi}{3}\right) \end{aligned} \tag{7}$$

In the equation, $\theta_{\mathrm{o}} = \omega_{\mathrm{o}} t$, and ω_{o} is the angular frequency of output voltage. We divide output voltage into 6 sectors as shown in Figure 3(c). By applying zero sequence to three-phase SPWM modulation wave, we can obtain the space vector modulation function with high-side or down-side switch clamped at DC bus in $\pi/3$ in (8).

In (8), $\mathrm{m_o}$ is the inverter modulation coefficient; $\mathrm{k_o}$ is the distribution coefficient of two output zero vectors of inverter, and it is equal to 1 and 0 at even and odd sectors, respectively; $\mathrm{u_{min}}$ and $\mathrm{u_{max}}$ are the minimum and maximum output phase voltages.

$$\begin{aligned} u_A^* &= m_o\left[\mathrm{u}_A - \mathrm{k}_o \mathrm{u}_{\min} - (1 - \mathrm{k}_o)\,\mathrm{u}_{\max}\right] + 1 - 2\mathrm{k}_o \\ u_B^* &= m_o\left[\mathrm{u}_B - \mathrm{k}_o \mathrm{u}_{\min} - (1 - \mathrm{k}_o)\,\mathrm{u}_{\max}\right] + 1 - 2\mathrm{k}_o \\ u_C^* &= m_o\left[\mathrm{u}_C - \mathrm{k}_o \mathrm{u}_{\min} - (1 - \mathrm{k}_o)\,\mathrm{u}_{\max}\right] + 1 - 2\mathrm{k}_o, \\ & m_o \in (0, 1.1547) \end{aligned} \tag{8}$$

This paper adopts this modulation function to reduce the number of inverter commutation. Figure 3(d) shows the waveform of inverter modulation function. Based on regular sampling principle, the duty ratio of three-phase high-side switches of inverter is [22–25]

$$\begin{aligned} d_A &= 0.5\left(1 + u_A^*\right) \\ d_B &= 0.5\left(1 + u_B^*\right) \\ d_C &= 0.5\left(1 + u_C^*\right) \end{aligned} \tag{9}$$

In one carrier period $\mathrm{T_s} = 1/f_{\mathrm{s}}$, the DC-side voltage consists of two different input line voltages, and the two corresponding action times is determined by (6). The inverter should take modulation in each action time of two line voltages, respectively. However, the modulation is not carried out in the whole line voltage action time but the first half of it according to (6), namely, the working vector action time of rectifier $\mathrm{d}_\alpha \mathrm{T_s}$ and $\mathrm{d}_\beta \mathrm{T_s}$. Therefore, the local average value of DC-side voltage utilized by inverter in one carrier period is equal to

$$\overline{u}_{pn} = d_\alpha u_1 + d_\beta u_2 = 1.5 U_{im} \tag{10}$$

In the equation, U_{im} is the maximum value of input phase voltage.

To make full use of the two line voltages, the same duty ratio of inverter should be adopted in two action times, which ensures the phase angle could stay same in one carrier period. Equation (10) shows that the average value of DC-side voltage utilized by inverter is constant; thus the calculation amount is reduced effectively, which differs from that of rectifier [26–28]. This is because the rectifier modulation technique has not zero vectors and then the formula needs real time correction.

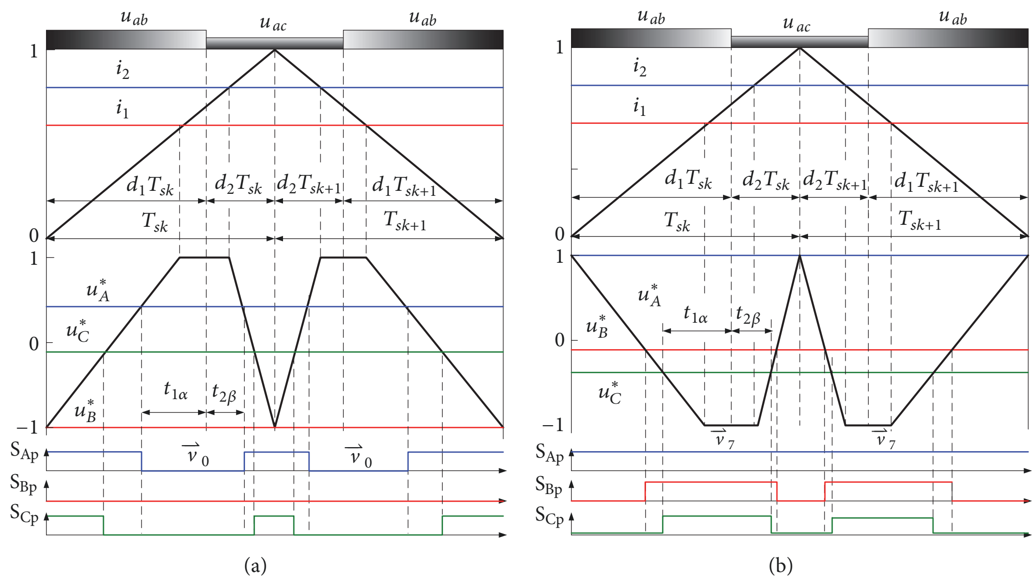

Figure 4: Modulation diagram of rectifier and inverter: (a) sector 1 and (b) sector 2.

In the collaborative modulation, the duty ratio formula of inverter when rectifier contains zero vectors is as follows:

$$d_{j\alpha} = d_j d_\alpha$$
$$d_{j\beta} = d_j d_\beta, \tag{11}$$
$$j \in (\mathrm{A}, \mathrm{B}, \mathrm{C})$$

Figure 4 shows the collaborative modulation of the first sector of rectifier. Because one phase of the inverter modulation function is -1 and 1 in odd and even sectors, respectively, different carriers are employed in odd and even inverter sectors. In adjacent carrier periods T_{sk} and T_{sk+1}, symmetrical trigonometric wave is employed as the carrier in rectifier. In each carrier period, the output line voltages of rectifier are u_{ab} and u_{ac} in d_1T_s and d_2T_s, respectively, and the commutation is carried out in rectifier ZVAT. In each period, it only commutates once and there is no commutation in period transition. In the working vector action time $d_\alpha T_s$ and $d_\beta T_s$, unilateral PWM is adopted in inverter. In ZVAT d_0T_s, $\mathbf{v_0}$ and $\mathbf{v_7}$ remain the same. Therefore, the inverter carrier wave shows the shape of scalene triangle with flat. The inverter commutates 4 times in each carrier period with no commutation in period transition. Thus, both rectifier and inverter avoid the unnecessary commutation.

The TSMC conventional modulation contains three constant frequencies, namely, f_s, f_0, and f_i, and the modulation has periodicity. The output voltage pulse can be represented by a triple Fourier series.

The phase voltage of the output A-phase is expressed as follows:

$$u_{\mathrm{AN}} = \sum_{l=-\infty}^{+\infty} \sum_{\mathrm{m}=-\infty}^{+\infty} \sum_{n=-\infty}^{+\infty} K_{lmn} e^{j(lr+ms+nz)} \tag{12}$$

In the formula, $r = \omega_s t$; $s = \omega_o t$; $z = \omega_s t$; $\omega_s = 2\pi f_s$; K_{lmn} is the $lf_s \pm mf_0 \pm nf_i$ harmonic coefficient.

Since the modulation function of phase B lags the phase A by $2\pi/3$, the triple Fourier series of the phase B voltage is

$$u_{\mathrm{BN}} = \sum_{l=-\infty}^{+\infty} \sum_{\mathrm{m}=-\infty}^{+\infty} \sum_{n=-\infty}^{+\infty} K_{lmn} e^{-j2m\pi 3^{-1}} e^{j(lr+ms+nz)} \tag{13}$$

Thus, the Fourier series of the line voltage $u_{\mathrm{AB}} = u_{\mathrm{AN}}$-$u_{\mathrm{BN}}$ is

$$u_{\mathrm{AB}} = \sum_{l=-\infty}^{+\infty} \sum_{\mathrm{m}=-\infty}^{+\infty} \sum_{n=-\infty}^{+\infty} K_{lmn} \left(1 - e^{-j2m\pi 3^{-1}}\right) e^{j(lr+ms+nz)} \tag{14}$$

The amplitude of the $lf_s \pm mf_0 \pm nf_i$ harmonic of the output voltage is as follows:

$$A_{lmn} = 2\left|K_{lmn}\left(1 - e^{-j2m\pi/3}\right)\right| \tag{15}$$

According to (15), the spectrum of the constant carrier frequency output line voltage u_{AB} as shown in Figure 5 is calculated by Matlab, wherein the input phase voltage amplitude is 100V, the frequency is 50 Hz, the output current frequency is 30 Hz, and the carrier frequency is 10 kHz. Since the rectification stage uses a symmetric triangular carrier in two adjacent carrier cycles, the output voltage harmonics contain discrete harmonics concentrated at around 5 kHz.

From the perspective of time domain analysis, the PWM pulse is formed by the pulse connection of different switching moments of a certain width [29–32]. The CCFMT is such that the carrier period changes with the modulation signal, resulting in a change of the switching time; from the perspective of frequency domain analysis, the PWM pulse is composed of discrete harmonics with fixed fundamental amplitude and frequency. CCFMT is to make the carrier frequency change with the modulation signal, independently spread the single frequency harmonic, and reduce its peak value [33].

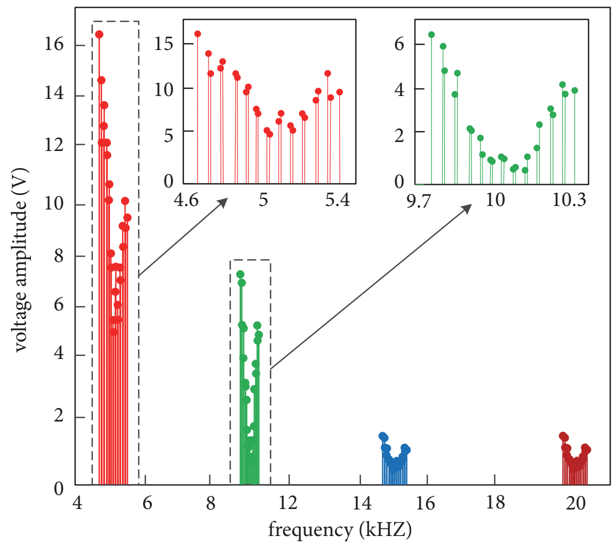

Figure 5: Output line voltage spectrum simulation diagram.

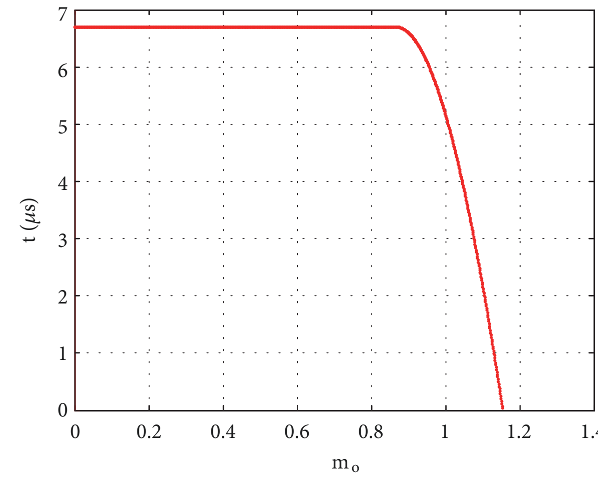

Figure 6: Relation between minimum commutation time and m_o.

According to the principle of conservation of harmonic energy, the wider the frequency bands of a single harmonic extension, the lower the amplitude. It can be seen from (1) that the larger the maximum frequency offset, the larger the range of carrier frequency variation, and the wider the harmonic spread after CCFMT modulation, the flatter the spectrum. However, since the adjacent discrete harmonic distribution pitch is much smaller than the extended frequency band, harmonic sidebands of different frequencies are likely to overlap. The amplitudes of the components with opposite phases at the same frequency cancel each other out, and the amplitudes of the components with the same phase are superimposed on each other, making the spectrum distribution quite complicated. However, the overall spectral overlap of the overlap will increase.

According to the constant carrier frequency modulation, the output voltage frequency at the maximum frequency offset frequency Δf_s=2 kHZ, 5 kHZ can also be obtained. The increase of Δf_s is more obvious.

The TSMC modulates the sinusoidal input and output current through the cooperative operation of the rectification stage and the inverter stage. The change of the current is determined by the applied pulse, so the modulated current has ripples of up and down jitter. The magnitude of the ripple is related to the pulse width of the action, and the pulse width is determined by the product of the duty cycle of each switch and the switching period. The duty cycle is related to the modulation wave and is independent of the carrier frequency. In constant carrier frequency modulation, the pulse width changes over and over again. In CCFMT, the pulse width changes in a chaotic manner, thus causing a chaotic change in current modulation time. In a carrier cycle, as the carrier period becomes larger, the current change time also increases, and the range of variation also increases. As the carrier cycle becomes smaller, the range of current variation also becomes smaller. The CCFMT changes the carrier frequency up and down around the center frequency, resulting in an increase in current ripple. The larger the range of carrier frequency variation, the larger the maximum frequency offset Δf_s, and the larger the range of current variation in one carrier period.

During one carrier cycle, the TSMC rectification stage is modulated by two line voltages, and the inverter stage is demodulated separately during the two line voltages. The pulse width of the rectification stage is affected by the change of the carrier frequency than the pulse width of the inverter stage, so the input current ripple is also affected by the CCFMT and larger than the output current ripple.

3. The Analysis on Narrow Pulses

In Figure 4, $t_{1\alpha}$ and $t_{2\beta}$ are rectifier commutation time. In $t_{1\alpha}$, the inverter outputs zero vector and the current of DC bus goes to zero, which prepares for zero current commutation of rectifier. In $t_{2\beta}$, the commutation of rectifier is carried out under the second principle modulating the output line voltage for the second stage of inverter. In $t_{1\alpha}$, a switch of inverter is turned off and the other switch of the same bridge is turned on after some dead-time; in $t_{2\beta}$, a bidirectional switch is turned off and the other switch is turned on after some dead-time; thus the needed commutation time is the same [34, 35, 42].

Figure 6 shows the relation between the minimum commutation time and m_o obtained by Matlab, and T_s=100μs. If m_o < 0.867, the minimum commutation time appears at the beginning and ending of rectifier sectors, and it is equal to the half of maximum ZVAT. If m_o > 0.867, with m_o increasing, the minimum commutation time moves toward middle and decreases at the same time. At last, it goes to zero at m_o=1.1547 in full-commutation. Then, to avoid narrow pulses, m_o should not be too large, and we prefer m_o=1. Thus, the minimum commutation time is 5.1713μs, and there is enough time for rectifier commutation to remove narrow pulses.

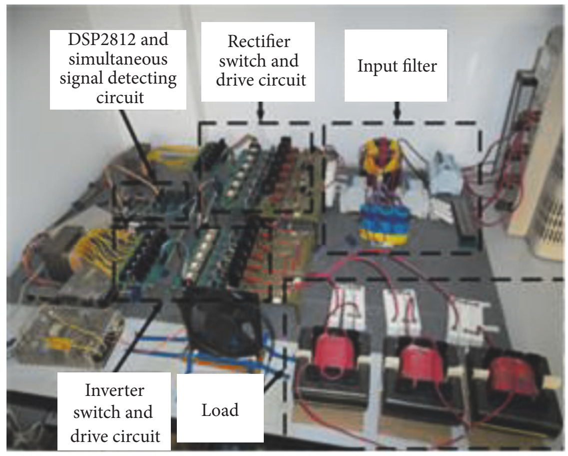

Figure 7: Experimental platform of TSMC.

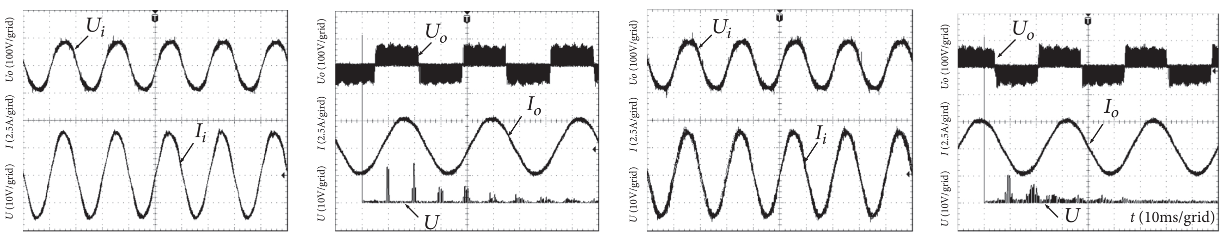

(a) (b) (c) (d)

Figure 8: (a) Waves of input phase voltage and input current (CFMT). (b) Waves of output line voltage and output current, and frequency spectrum of output line voltage (CFMT). (c) Waves of input phase voltage and input current (CCFMT). (d) Waves of output line voltage and output current, and frequency spectrum of output line voltage (CCFMT).

4. The Experiment Result

To verify the effectiveness of CCFMT, the TSMC experiment platform is built in Figure 7. The controller is DSP2812. The amplitude of input phase voltage is 100V and the frequency is 50Hz. The parameters of input RLC filter are L=2mH, C=10μF, and R=200Ω; the Y-connection load is made up of 10Ω resistors and 6mH inductors in series; the constant carrier frequency is 10kHz, and the maximum offset is 2kHz; the dead-time is 2μs. The result is measured by Tektronix oscilloscope TDS3032B with probe P5205 and TCPA300. In Figure 8, because the carrier frequency in Figure 8(c) changes according to chaotic principle, the fluctuation of input current and voltage is larger than that in Figure 8(a). In addition, from Figures 8(b) and 8(d), both modulations can bring about commendable waves of output voltage and current. However, in constant carrier frequency modulation, the harmonics in output line voltage frequency spectra concentrate on integer multiples of carrier frequency (because the symmetric triangular carrier is adopted in rectifier, the actual carrier frequency is halved) and possess large peak values bringing about powerful EMI. In chaotic carrier frequency modulation, the sideband range is spread and peak values are reduced effectively without changing the fundamental component. Furthermore, the sideband is spread more widely with the frequency increasing, which makes the harmonic distribution evenly and suppresses EMI.

Table 1: HSF of output voltages from fixed CFMT and CCFMT with different $\triangle f_s$.

$\triangle f_s$/kHZ	0	2	3	4	5
HSF	0.85	0.7	0.68	0.66	0.64

In order to evaluate the effect of $\triangle f_s$ on the spread spectrum effect, the concept of variance in statistics is introduced to define the harmonic expansion factor (HSF). HSF can quantitatively describe the spread spectrum effect. HSF can quantitatively describe the spread spectrum effect. If the HSF is smaller, the harmonic spectrum is flatter. Table 1 shows the HSF of the output voltage spectrum for a constant carrier frequency and CCFMT at different Δf_s modulations.

5. Conclusions

This paper first proposed the application of CCFMT to TSMC. The proposed new CCFMT can effectively improve the reliability of commutation, solve the narrow pulse problem, and simplify the commutation process. By changing the carrier frequency, extending the harmonic spectrum, and reducing the peak value of the output voltage harmonics, EMI is effectively suppressed. In addition, the effectiveness of CCFMT was proved by experiments. However, CCFMT will increase the input current ripple and still need improvement in future research.

Data Availability

The data used to support the findings of this study are available from the corresponding author upon request.

Conflicts of Interest

The authors declare that there are no conflicts of interest regarding the publication of this article.

Acknowledgments

The work was supported by the Qingdao Postdoctoral Fund (No. 2015118) and Key Research, the Development Plan of Shandong Province (No. 2017GGX50114 and No. 2018GGX105007), and the Scientific Research Development Plan of Shandong Higher Education Institutions (No. J18KA316).

References

[1] K. Yin, S. Yang, X. Dong, D. Chu, X. Gong, and J. Duan, "Femtosecond laser fabrication of shape-gradient platform: underwater bubbles continuous self-driven and unidirectional transportation," *Applied Surface Science*, vol. 471, pp. 999–1004, 2019.

[2] Y. Sun, X. Li, M. Su, H. Wang, H. Dan, and W. Xiong, "Indirect matrix converter-based topology and modulation schemes for enhancing input reactive power capability," *IEEE Transactions on Power Electronics*, vol. 30, no. 9, pp. 4669–4681, 2015.

[3] T. H. Huang and K. L. Lian, "Harmonic modeling of a diode-clamped multilevel voltage source converter for predicting uncharacteristic harmonics," *Mathematical Problems in Engineering*, vol. 2018, Article ID 3250761, 16 pages, 2018.

[4] K. Wang, J. Pang, L. Li, S. Zhou, Y. Li, and T. Zhang, "Synthesis of hydrophobic carbon nanotubes/reduced graphene oxide composite films by flash light irradiation," *Frontiers of Chemical Science and Engineering*, vol. 12, no. 3, pp. 376–382, 2018.

[5] Y. Fu, J. Ding, H. Wang, and J. Wang, "Two-objective stochastic flow-shop scheduling with deteriorating and learning effect in Industry 4.0-based manufacturing system," *Applied Soft Computing*, vol. 68, pp. 847–855, 2018.

[6] R. Wang, X. Mu, Z. Wu, L. Zhu, Q. Chen, and X. Wang, "Carrier-based PWM method to reduce common-mode voltage of three-to-five-phase indirect matrix converter," *Mathematical Problems in Engineering*, vol. 2016, Article ID 6086497, 10 pages, 2016.

[7] Y. Fu, G. Tian, Z. Li, and Z. Wang, "Parallel machine scheduling with dynamic resource allocation via a master–slave genetic algorithm," *IEEJ Transactions on Electrical and Electronic Engineering*, vol. 13, no. 5, pp. 748–756, 2018.

[8] Q. Sun, Y. Wang, J. Yang, Y. Qiu, and H. Zhang, "Chaotic dynamics in smart grid and suppression scheme via generalized fuzzy hyperbolic model," *Mathematical Problems in Engineering*, vol. 2014, Article ID 761271, 7 pages, 2014.

[9] W. Chen, Z.-C. He, G.-B. Huang, C.-L. Wu, W.-F. Chen, and X.-H. Liu, "Direct Z-scheme 2D/2D MnIn2S4/g-C3N4 architectures with highly efficient photocatalytic activities towards treatment of pharmaceutical wastewater and hydrogen evolution," *Chemical Engineering Journal*, vol. 359, pp. 244–253, 2019.

[10] D. Zeng, Y. Qiu, S. Peng et al., "Enhanced hydrogen production performance through controllable redox exsolution within CoFeAlO: X spinel oxygen carrier materials," *Journal of Materials Chemistry A*, vol. 6, no. 24, pp. 11306–11316, 2018.

[11] X. -T Xu, A. Enaiet-Allah, C. Wang et al., "Capacitive deionization using nitrogen-doped mesostructured carbons for highly efficient brackish water desalination," *Chemical Engineering Journal*, vol. 362, pp. 887–896, 2019.

[12] F. Wu, F. Feng, L. Luo, J. Duan, and L. Sun, "Sampling period online adjusting-based hysteresis current control without band with constant switching frequency," *IEEE Transactions on Industrial Electronics*, vol. 62, no. 1, pp. 270–277, 2015.

[13] L. Yu and Y. Li, "A flexible-possibilistic stochastic programming method for planning municipal-scale energy system through introducing renewable energies and electric vehicles," *Journal of Cleaner Production*, vol. 207, pp. 772–787, 2019.

[14] A. Garcés and M. Molinas, "A study of efficiency in a reduced matrix converter for offshore wind farms," *IEEE Transactions on Industrial Electronics*, vol. 59, no. 1, pp. 184–193, 2012.

[15] G. Yang, J. Wang, H. Zhang, H. Jia, Y. Zhang, and F. Gao, "Applying bio-electric field of microbial fuel cell-upflow anaerobic sludge blanket reactor catalyzed blast furnace dusting ash for promoting anaerobic digestion," *Water Research*, vol. 149, pp. 215–224, 2019.

[16] K. Wang, L. Zhang, B. Ji, and J. Yuan, "The thermal analysis on the stackable supercapacitor," *Energy*, vol. 59, pp. 440–444, 2013.

[17] J. Luo, D. Song, C. Xiu, S. Geng, and T. Dong, "Fingerprint classification combining curvelet transform and gray-level cooccurrence matrix," *Mathematical Problems in Engineering*, vol. 2014, Article ID 592928, 15 pages, 2014.

[18] K. Wang, S. Z. Zhou, Y. T. Zhou, J. Ren, L. W. Li, and Y. Lan, "Synthesis of porous carbon by activation method and its electrochemical performance," *International Journal of Electrochemical Science*, vol. 13, no. 11, pp. 10766–10773, 2018.

[19] N. Li, S. Tang, Y. Rao, J. Qi, Q. Zhang, and D. Yuan, "Peroxymonosulfate enhanced antibiotic removal and synchronous electricity generation in a photocatalytic fuel cell," *Electrochimica Acta*, vol. 298, pp. 59–69, 2019.

[20] S. Tang, D. Yuan, Y. Rao et al., "Percarbonate promoted antibiotic decomposition in dielectric barrier discharge plasma," *Journal of Hazardous Materials*, vol. 366, pp. 669–676, 2019.

[21] N. Li, S. Tang, Y. Rao et al., "Improved dye removal and simultaneous electricity production in a photocatalytic fuel cell coupling with persulfate activation," *Electrochimica Acta*, vol. 270, pp. 330–338, 2018.

[22] L. Kang, H. L. Du, H. Zhang, and W. L. Ma, "Systematic research on the application of steel slag resources under the background of big data," *Complexity*, vol. 2018, Article ID 6703908, 12 pages, 2018.

[23] C. Duan, J. Huo, F. Li, M. Yang, and H. Xi, "Ultrafast room-temperature synthesis of hierarchically porous metal–organic frameworks by a versatile cooperative template strategy," *Journal of Materials Science*, vol. 53, no. 24, pp. 16276–16287, 2018.

[24] P. Li, Z. Han, X. Jia, Z. Mei, X. Han, and Z. Wang, "Analysis and comparison on thermodynamic and economic performances of an organic Rankine cycle with constant and one-dimensional

dynamic turbine efficiency," *Energy Conversion and Management*, vol. 180, pp. 665–679, 2019.

[25] Y. Yang, H. Li, W. Zheng, Y. Bai, Z. Liu, and J. Zhang, "Experimental study on calcining process of secondary coated ceramsite solidified chromium contaminated soil," *Science of Advanced Materials*, vol. 11, no. 2, pp. 208–214, 2019.

[26] W. Kai, L. Liwei, X. Wen et al., "Electrodeposition synthesis of PANI/MnO2/graphene composite materials and its electrochemical performance," *International Journal of Electrochemical Science*, vol. 12, no. 9, pp. 8306–8314, 2017.

[27] L. Niu, J. L. Xu, W. L. Yang, C. H. Kang, J. Q. Ma, and J. Q. Su, "Synergistic effect between nano-Sb_2O_3 and brominated epoxy resin on the flame retardancy of poly(butylene terephthalate)," *Science of Advanced Materials*, vol. 11, no. 5, 2019.

[28] J.-X. Sui, X.-X. Wang, C. Song, Q. Liu, F. Yuan, and Y.-Z. Long, "Preparation and low-temperature electrical and magnetic properties of $La_{0.33}Pr_{0.34}Ca_{0.33}MnO_3$ nanofibers via electrospinning," *Journal of Magnetism and Magnetic Materials*, vol. 467, pp. 74–81, 2018.

[29] Q. Sun, Y. Yang, Z. Zhao et al., "Elaborate design of polymeric nanocomposites with Mg(ii)-buffering nanochannels for highly efficient and selective removal of heavy metals from water: case study for Cu(ii)," *Environmental Science: Nano*, vol. 5, no. 10, pp. 2440–2451, 2018.

[30] C. Duan, F. Li, J. Xiao, Z. Liu, C. Li, and H. Xi, "Rapid room-temperature synthesis of hierarchical porous zeolitic imidazolate frameworks with high space-time yield," *Science China Materials*, vol. 60, no. 12, pp. 1205–1214, 2017.

[31] Y. Fu, H. Wang, G. Tian, Z. Li, and H. Hu, "Two-agent stochastic flow shop deteriorating scheduling via a hybrid multi-objective evolutionary algorithm," *Journal of Intelligent Manufacturing*, 2018.

[32] K. Wang, L. Li, T. Zhang, and Z. Liu, "Nitrogen-doped graphene for supercapacitor with long-term electrochemical stability," *Energy*, vol. 70, pp. 612–617, 2014.

[33] H. Li, K. Shin, and G. Henkelman, "Effects of ensembles, ligand, and strain on adsorbate binding to alloy surfaces," *The Journal of Chemical Physics*, vol. 149, Article ID 174705, 8 pages, 2018.

[34] K. Wang, C. Li, and B. Ji, "Preparation of electrode based on plasma modification and its electrochemical application," *Journal of Materials Engineering and Performance*, vol. 23, no. 2, pp. 588–592, 2014.

[35] H. Li, L. Luo, P. Kunal et al., "Oxygen reduction reaction on classically immiscible bimetallics: a case study of RhAu," *The Journal of Physical Chemistry C*, vol. 122, no. 5, pp. 2712–2716, 2018.

[36] J. Wang, S. Zhou, Z. Zhang, and D. Yurchenko, "High-performance piezoelectric wind energy harvester with Y-shaped attachments," *Energy Conversion and Management*, vol. 181, pp. 645–652, 2019.

[37] F. Wang, Q. Hua, and C.-S. Liu, "Boundary function method for inverse geometry problem in two-dimensional anisotropic heat conduction equation," *Applied Mathematics Letters*, vol. 84, pp. 130–136, 2018.

[38] W. Z. Qu, W. Chen, and Y. Gu, "Fast multipole accelerated singular boundary method for the 3D Helmholtz equation in low frequency regime," *Computers & Mathematics with Applications*, vol. 70, no. 4, pp. 679–690, 2015.

[39] F. Wang, C.-S. Liu, and W. Qu, "Optimal sources in the MFS by minimizing a new merit function: energy gap functional," *Applied Mathematics Letters*, vol. 86, pp. 229–235, 2018.

[40] W. Qu and W. Chen, "Solution of two-dimensional Stokes flow problems using improved singular boundary method," *Advances in Applied Mathematics and Mechanics*, vol. 7, no. 1, pp. 13–30, 2015.

[41] S. Zhou and J. Wang, "Dual serial vortex-induced energy harvesting system for enhanced energy harvesting," *AIP Advances*, vol. 8, no. 7, Article ID 075221, 10 pages, 2018.

[42] H. Li and G. Henkelman, "Dehydrogenation selectivity of ethanol on close-packed transition metal surfaces: a computational study of monometallic, Pd/Au, and Rh/Au catalysts," *The Journal of Physical Chemistry C*, vol. 121, no. 49, pp. 27504–27510, 2017.